The Astrophysical Journal, 573:720–727, 2002 July 10

SUBARCSECOND MID-INFRARED IMAGING OF TWO POST–ASYMPTOTIC GIANT BRANCH 21 MICRON SOURCES[1]

Sun Kwok[2] and Kevin Volk
Department of Physics and Astronomy, University of Calgary, Calgary, ABT 2N 1N4, Canada; kwok@iras.ucalgary.ca, volk@iras.ucalgary.ca

and

Bruce J. Hrivnak
Department of Physics and Astronomy, Valparaiso University, Valparaiso, IN 46383; bruce.hrivnak@valpo.edu
Received 2001 September 5; accepted 2002 March 12

ABSTRACT

High-resolution (FWHM 0.″4) mid-infrared images have been obtained for two proto–planetary nebulae possessing the 21 μm emission feature (IRAS 07134+1005 and Z02229+6208). Images through five filters were obtained, covering the 11.3 and 21 μm emission features as well as the adjacent dust continuum. The images of IRAS 07134+1005 show a clearly resolved shell structure, but no significant variation in morphology is seen between the different filters. The uniform morphology between the emission features and the continuum suggests that both the carriers of the 11.3 μm aromatic band and the 21 μm feature originate from the material ejected during the asymptotic giant branch phase of evolution.

Subject headings: circumstellar matter — infrared: stars — ISM: lines and bands — planetary nebulae: general — stars: AGB and post-AGB

1. INTRODUCTION

The identity of a strong emission feature at 21 μm in a number of proto–planetary nebulae (PPNs) is one of the most interesting unresolved mysteries in astrochemistry. Following the initial discovery of four sources (Kwok, Volk, & Hrivnak 1989), there are now 12 sources known to have this feature (Kwok, Hrivnak, & Geballe 1995; Kwok, Volk, & Hrivnak 1999b). All of the 21 μm sources are found to be F or G supergiants with large infrared excesses. These sources are found to be carbon-rich based on the presence of C_2, C_3, and CN molecular bands in their visible spectra (Hrivnak 1995; Bakker et al. 1997). High-resolution visible spectroscopy of the 21 μm sources has shown that all sources have enhanced *s*-process elements, indicating that they have gone through the third dredge-up on the asymptotic giant branch (AGB) and are definitely objects in the post-AGB phase of evolution (van Winckel & Reyniers 2000).

Also present in their infrared spectra are the 3.3, 6.2, 7.7, 8.6, and 11.3 μm emission features, which are attributed to various stretching and bending modes of aromatic hydrocarbons. These aromatic infrared bands (AIB) stand on top of two broad emission plateaus at 8 and 12 μm (Hrivnak, Volk, & Kwok 2000), which are likely to be due to emissions from a variety of aliphatic side groups attached to the aromatic rings (Kwok, Volk, & Bernath 2001). Below these emission features is a broad continuum stretching from near-infrared to submillimeter wavelengths, which probably originates from a solid-state substance (e.g., amorphous carbon).

Many candidates have been proposed as the carrier of the 21 μm feature, including hydrogenated amorphous carbon (Buss et al. 1990; Grishko et al. 2001), hydrogenated fullerences (Webster 1995), nanodiamonds (Hill, Jones, & d'Hendecourt 1998), TiC nanoclusters (von Helden et al. 2000), and O-substituted five-member carbon rings (Papoular 2000). Although there is no definite identification, the carbon-rich nature of the sources makes it likely that the 21 μm feature arises from a carbon-based compound.

While spectroscopic observations by the *Infrared Space Observatory* (*ISO*) have provided excellent data on the strengths, peak wavelength, and emission profile of the 21 μm feature in PPNs (Volk, Kwok, & Hrivnak 1999), the spatial distribution of the emission feature in the circumstellar envelope is virtually unknown. There have been several previous efforts to image PPNs in the mid-infrared, and some emission regions have been spatially resolved (Meixner et al. 1997; Dayal et al. 1998; Jura, Chen, & Werner 2000). The new infrared-optimized Gemini telescopes have the capability to perform subarcsecond imaging in the mid-infrared and therefore offer the possibility of spatially resolving the emitting regions of the different emission features. With this in mind, mid-infrared images have been obtained of two PPNs that display the 21 μm emission feature with the goal of comparing the spatial distributions of the 21 μm feature, the AIBs, and the plateau continuum to investigate the possible origins of these features.

2. OBSERVATION

Observations were made at the Gemini North Telescope on 2000 December 2 (for IRAS Z02229+6208) and December 7 (for IRAS 07134+1005=HD 56126) under the

[1] This paper is based on observations obtained at the Gemini Observatory, which is operated by the Association of Universities for Research in Astronomy, Inc., under a cooperative agreement with the NSF on behalf of the Gemini partnership: the National Science Foundation (United States), the Particle Physics and Astronomy Research Council (United Kingdom), the National Research Council (Canada), CONICYT (Chile), the Australian Research Council (Australia), CNPq (Brazil), and CONICET (Argentina). The observations were made with the mid-infrared camera OSCIR, developed by the University of Florida with support from the National Aeronautics and Space Administration and operated jointly by Gemini and the University of Florida Infrared Astrophysics Group.

[2] Canada Council Killam Fellow.

QUICKSTART program using the OSCIR instrument built by the University of Florida. OSCIR consists of a 128×128 Si:As IBC detector array and is capable of performing 8–25 μm imaging and low/medium ($R \sim 100$–1000) resolution spectroscopy. On Gemini, OSCIR has a plate scale of $0\farcs089$ pixel^{-1} and a total field of view in its imaging configuration of $11'' \times 11''$. Observations were taken in the imaging mode in five filters: 10.3 ($\Delta\lambda = 1.1$ μm), 11.7 ($\Delta\lambda = 1.1$ μm), 12.5 ($\Delta\lambda = 1.2$ μm), 18.2 ($\Delta\lambda = 1.7$ μm), and 20.8 μm ($\Delta\lambda = 1.7$ μm).

Observations were made with the telescope active optics, using an elevation-dependent lookup table. Telescope guiding was done with the secondary mirror making fast "tip-tilt" corrections of 20 Hz using guide stars acquired using the peripheral wavefront sensors. Based on observations of the standard β Peg, we derived an estimated image FWHM of $0\farcs39$ in the N band and $0\farcs75$ in the Q band. The standard mid-infrared technique of chopping (the secondary) and nodding (the telescope) was used to achieve accurate sky and telescope background cancellation. The chopping was done at 3 Hz with a $15''$ displacement in the north-south direction. The on-source integration times were between 3 and 10 minutes.

The images were flux calibrated using the *ISO* SWS01 spectrum of each source; these are expected to have an absolute photometric accuracy of about 10%. For each filter, the *ISO* spectrum was integrated over the OSCIR filter profile to produce an expected in-band total flux in Jy. From the images, the IRAF task *imexamine* was used to derive the total counts over an aperture slightly larger than the object. By equating the total counts to the in-band flux and making use of the known pixel scale of OSCIR, we derived absolute brightness values in Jy arcsec^{-2} for each of the images.

As a result of the continuous sky subtraction carried out through chopping and nodding, the background brightness away from the source in the OSCIR images is consistent with zero, and no further background subtraction was required.

Other than a small color term resulting from the difference in observing inside (Gemini) and outside (*ISO*) of the atmosphere, this process is accurate as long as the source is nonvariable. There is no evidence for variability, since the *IRAS* Low Resolution Spectrometer (calibrated by the PSC) and the *ISO* SWS01 observations show good agreement in shape and in absolute level for these two objects. Since the filters are all relatively narrow and the object spectra do not vary much over them, the color term will be small.

3. RESULTS

The reduced images of IRAS 07134+1005 and Z02229+6208 are shown in Figures 1 and 2, respectively. The central star of IRAS 07134+1005 is detected clearly in the 10.3 μm filter image and marginally in the 11.7 and 12.5 μm images. The dust shell of IRAS 07134+1005 is resolved in all filters and appears round. For IRAS Z02229+6208, the shell is marginally resolved and definitely elongated in the northeast-southwest direction. The only anomaly is the 18 μm image, which seems to show a different orientation in the low-level contours. Perhaps this difference is due to variability in weather conditions. Using the four other images of IRAS Z02229+6208, the measured ellipticity is $\sim$0.15 with a position angle of 20°.

Figure 3 displays the 20.8 μm image of Z02229+6208 as logarithmic contours, showing that the dust emission extends as far as $2''$ from the central star. The FWHM size of the central region of Z02229+6208 is $\sim 0\farcs8$ in all five images, with a variation of $\sim$1.5%. When deconvolved with the OSCIR beam, this size implies an emission region with a FWHM size of $0\farcs7$.

In each of the five images of IRAS 07134+1005, a clear shell-like structure is seen. These are similar to the dust shells seen in high-resolution images of the planetary nebulae NGC 7027 and BD +30°3639 (K. Volk & S. Kwok 2002, in preparation). The shell structures are very similar between images with the different bandpasses, with an inner radius of $0\farcs8$ and an outer radius of $1\farcs2$. The dust shell is brightest in the southeast corner and has a peak surface brightness of 8.1 Jy arcsec^{-2} at 18.0 μm compared to the mean shell brightness of 5.4 Jy arcsec^{-2}.

4. DISCUSSION

4.1. *Feature Distribution*

As can be seen by comparison with the *ISO* spectrum of IRAS 07134+1005, the five filter bandpasses correspond approximately to emissions due to the continuum (10.3 μm), the aromatic C-H bending mode (11.7 μm), the plateau continuum (12.5 μm), the continuum (18.2 μm), and the 21 μm emission feature (20.8 μm). This is illustrated in Figure 4. One can see that the 21 μm feature is very strong and lies almost entirely within the 20.8 μm OSCIR bandpass. If the feature emission region is distributed differently than the continuum emission region, it should be easily detectable.

In order to map the differences in the distributions of the various emission features, we have created ratio and difference images using the absolutely calibrated images of IRAS 07134+1005. The ratioed maps (11.7/10.3 and 20.8/18.0) show completely flat images with pixel-to-pixel variations consistent with pure noise. Figure 5 shows the difference images for the 11.7–10.3 and the 20.8–18.0 images. The fact that the ratioed images are flat and the difference images appear to have the same morphology as the original images suggests that the 11.3 μm AIB and the 21 μm features are distributed no differently than the continuum emission. Thus, the carriers of these features appear to have no preferential distribution with respect to the continuum dust.

It has been suggested that if the 21 μm feature is due to TiC, then the necessary physical conditions require a sudden mass ejection at the end of the AGB with a mass-loss rate of 10^{-3} $M_\odot$ yr^{-1} (von Helden et al. 2000). From the observations presented here, we cannot detect any significant difference between the spatial distribution of the 21 μm emission, the AIB emission, and the plateau continuum emission. It is therefore conceivable that all of these emission features arise from the same species, or from different species ejected at the same time and well mixed at present, or from different species that have evolved chemically from materials that were ejected together during the AGB. While there is strong evidence that chemical synthesis is still ongoing during the post-AGB evolution (Kwok, Volk, & Hrivnak 1999a), our observations suggest that the ingredients of the AIB and 21 μm carriers were all ejected at the same time.

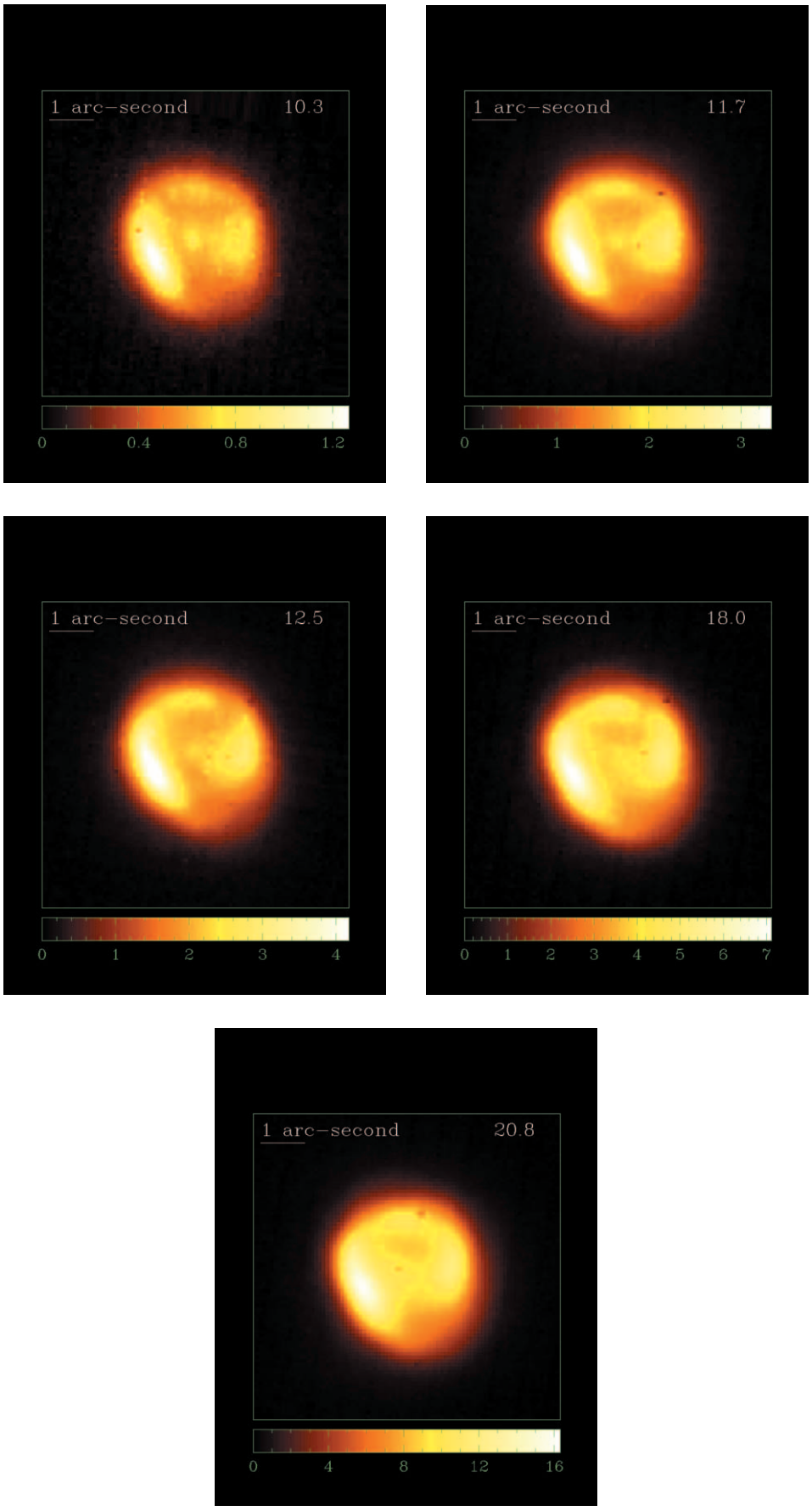

FIG. 1.—Infrared images of IRAS 07134+1005 at 10.3, 11.7, 12.5, 18.2, and 20.8 μm. All images have been absolutely calibrated, and the intensity scale (in Jy arcsec^{-2}) is given under each image. A size scale of 1″ is also plotted in each image. North is up and east to the left.

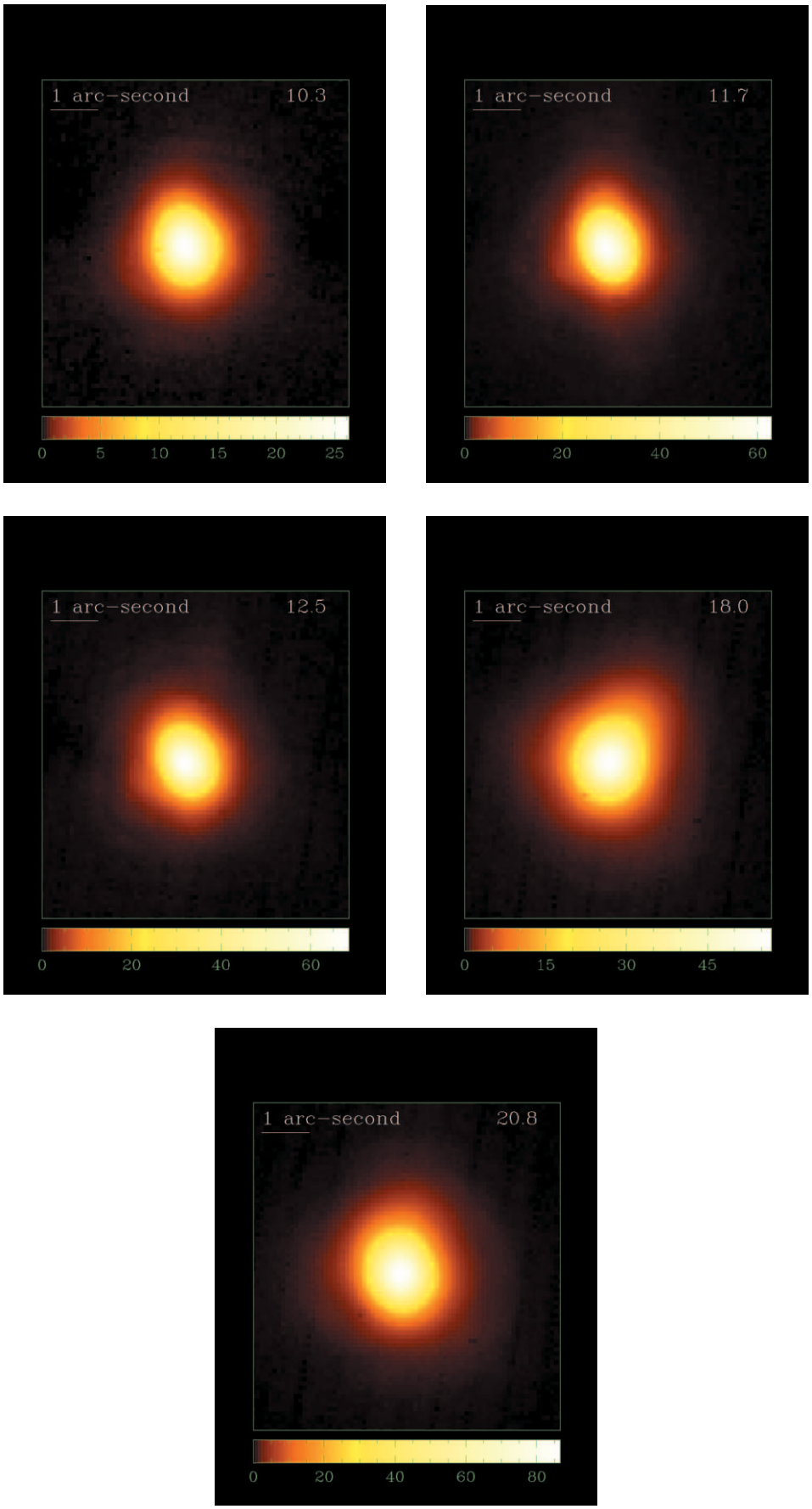

FIG. 2.—Infrared images of IRAS Z02229+6208 at 10.3, 11.7, 12.5, 18.2, and 20.8 μm shown on a square-rooted intensity scale. All images have been absolutely calibrated, and the intensity scale (in Jy arcsec^{-2}) is given under each image. A size scale of 1″ is also plotted in each image. North is up and east to the left.

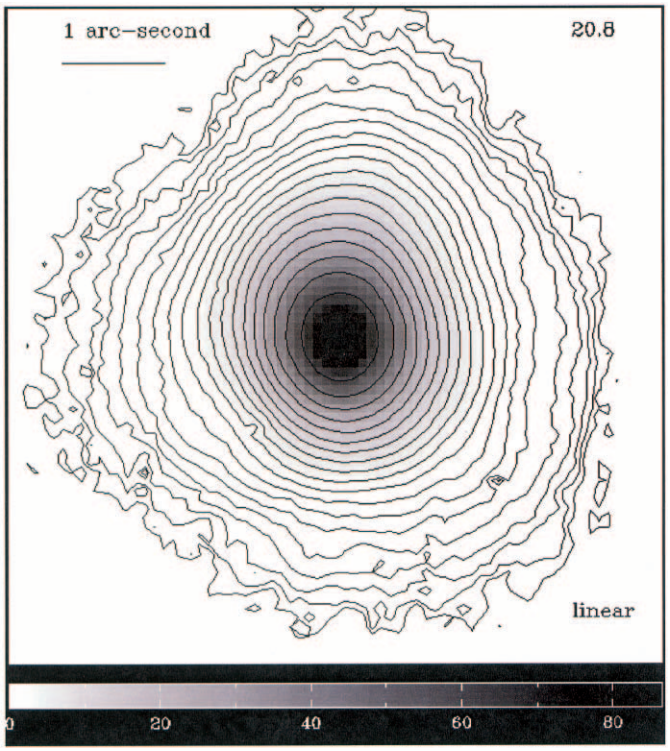

FIG. 3.—Logarithmically spaced contours overlaid on the 20.8 μm image (shown in a linear intensity scale) of IRAS Z02229+6208. The contour levels range from 0.22 to 85 Jy arcsec^{-2}.

4.2. *Morphology of the Dust Shell*

These infrared images show that the dust distribution in IRAS 07134+1005, to the first order, has a shell-like structure. In addition to the shell, two bright blobs can be seen in the images, a brighter one located to the east-southeast of the star and a less bright one to the west. The peak flux ratios between them are 1.53 at 11.7 μm and 1.37 at 20 μm. These two blobs had been seen in the lower resolution images of Meixner et al. (1997), Dayal et al. (1998), and Jura et al. (2000), but their relationship with the shell is seen much more clearly in the present observations (Fig. 1). Such double-peaked morphology is commonly seen in radio images of planetary nebulae and can be modeled well by an ellipsoidal shell with a latitude-dependent density gradient viewed at an angle (Aaquist & Kwok 1996). In cases of an extreme density gradient, such a structure can be described as a torus.

Figure 6 shows an overlay of the contours of the *HST* Wide Field Planetary Camera 2 (WFPC2) *V*-band image onto the 10.3 μm image. These two images were aligned easily by the positions of the central star and the rotation of the WFPC2 image according to the header information. The reflection nebula, as seen in the lower contours of the *HST* image, is slightly more extended than the infrared emission from the dust shell. If the two bright blobs represent an equatorial torus, then the optical reflection nebulosity could represent the front and back bipolar lobes projected onto the plane of the sky (Bryce, Balick, & Meaburn 1994). If such toroidal dust structures are common in PPNs, then they may play an important role in the shaping of PNs into bipolar forms.

The clear separation between the shell and the star suggests that the shell is the product of AGB mass loss that terminated in the recent past. This is consistent with the observed spectral energy distributions (SEDs) of PPNs, which generally show a double-peaked distribution characteristic of detached dust shells (Kwok 1993). We have fitted the SEDs of IRAS Z02229+6208 and IRAS 07134+1005 with one-dimensional radiation transfer models. Assuming a distance of 2 kpc, we derived a mass-loss rate of 6.0×10^{-5} ($V_{\rm exp}$/10 km s^{-1}) $M_\odot$ yr^{-1}, a luminosity of 6800 $L_\odot$, and a time lapse of 670 ($V_{\rm exp}$/10 km s^{-1})$^{-1}$ yr since the end of mass loss for Z02229+6208. Similarly, assuming a distance of 2 kpc, the SED of IRAS 07134+1005 can be fitted by a mass-loss rate of 3.6×10^{-5} ($V_{\rm exp}$/10 km s^{-1}) $M_\odot$ yr^{-1}, a luminosity of 5600 $L_\odot$, and a time lapse of 1080 ($V_{\rm exp}$/10 km

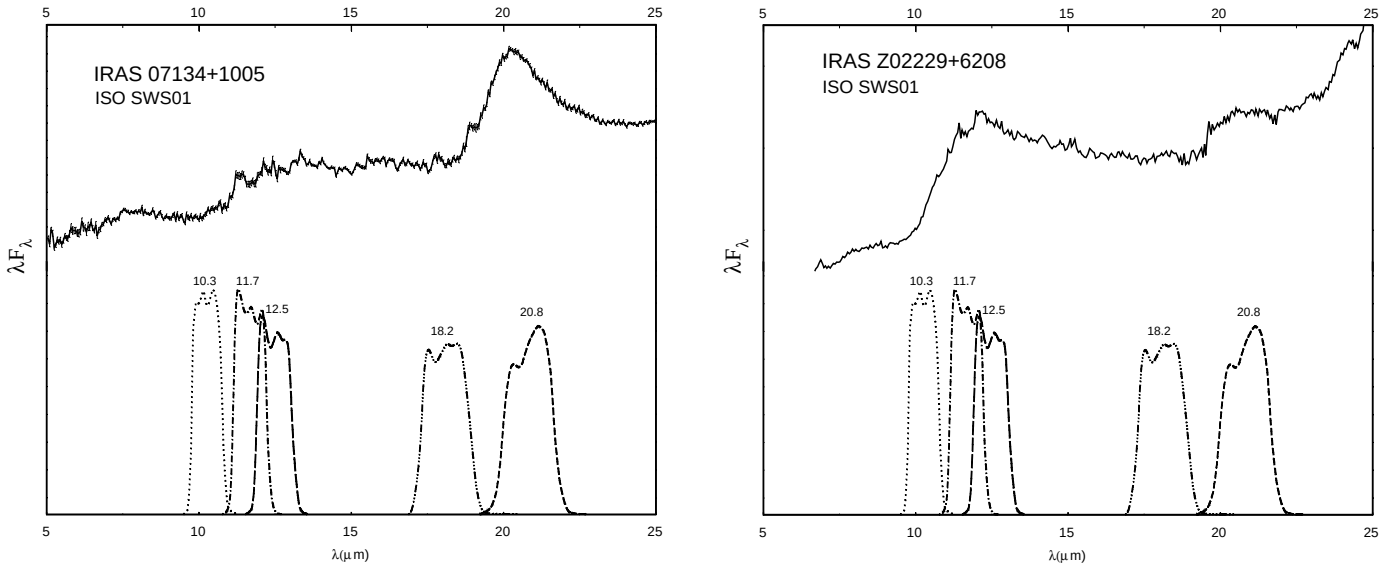

FIG. 4.—*ISO* spectra of IRAS 07134+1005 and IRAS Z02229+6208 (Hrivnak et al. 2000), plotted together with the profiles of five OSCIR filters used in the observations.

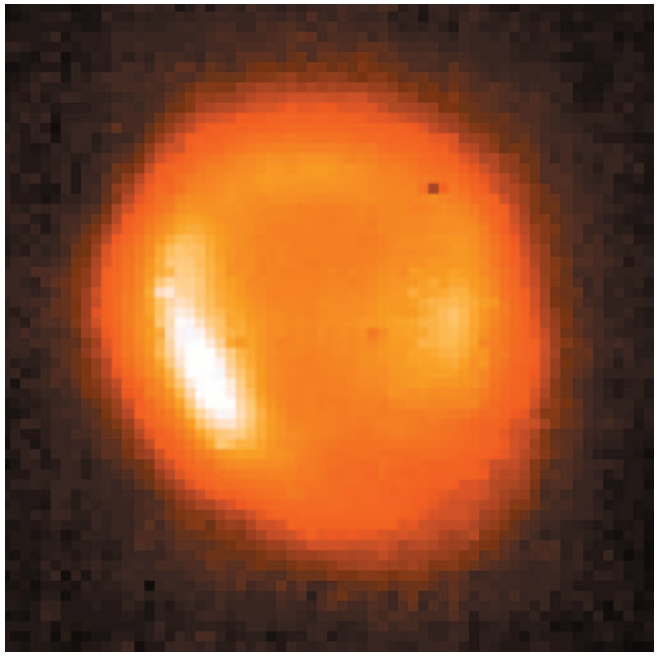

FIG. 5*a*

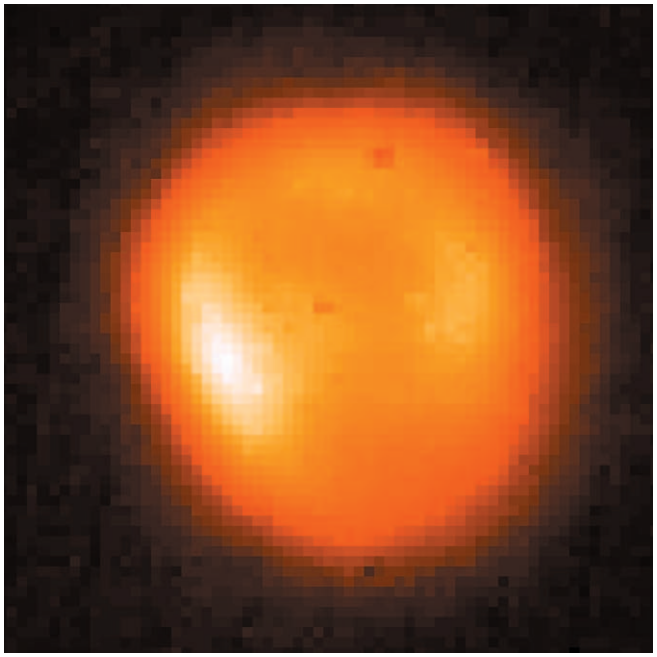

FIG. 5*b*

FIG. 5.—The (*a*) 11.7 − 10.3 and (*b*) 20.8 − 18.0 difference images of IRAS 07134+1005 after correction for flux ratios (from the *ISO* spectrum) and OSCIR filter profiles. The 11.3 and 21 μm features should appear in white in (*a*) and (*b*), respectively.

$s^{-1})^{-1}$ yr since the end of mass loss (Hrivnak et al. 2000; B. J. Hrivnak, K. Volk, & S. Kwok 2002, in preparation).

A comparison of the 10.6 μm one-dimensional model images to the absolutely calibrated observed 10.3 μm images is displayed in Figure 7. It can be seen that the model images are good approximations to the observed images. This is particularly striking when one realizes that the models were produced to fit the mid-infrared spectra and SEDs of these objects, without any prior knowledge of the brightness distribution of the dust shells. Since the shell of IRAS 07134+1005 is well resolved in the present observations, the observed intensity profile can be quantitatively compared with the model. The model predicts that the inner edge of the shell is located at 0.012 pc from the star, or an angular separation of 1″.2 (independent of assumed distance). This agrees well with the actual observed shell radius of 0″.8–1″.2 (§ 3).

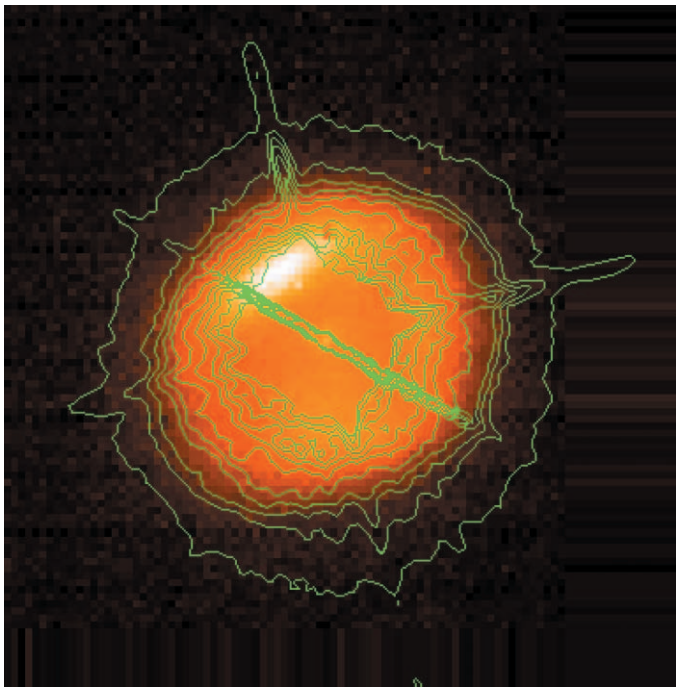

FIG. 6.—*HST* WFPC2 *V*-band image (shown as contours) of IRAS 07134+1005 overlaid on the 10.3 μm image. Note that this figure is oriented 49° clockwise with respect to Fig. 1. The streaks in the *HST* image are due to the saturated central star, and the diffraction pattern is seen. Only the lowest contours corresponding to the reflection nebula are plotted.

Although not plotted in Figure 7, the predicted flux of the central star is consistent with the observed brightness of the star at 10 μm when the observed stellar image is integrated over the PSF. The differences (∼20%) between the model and observed fluxes of the central star are within the uncertainties of the interstellar extinction values used to correct for the *V*-band flux of the star.

Figure 8 shows the model intensity profile of IRAS 07134+1005 in comparison with the observed intensity profiles in two directions. The model matches well with the basic size and intensity of the observed image. Differences exist as a result of the observed brightness peak of the shell on the eastern side and the observed higher intensity toward the projected center of the image. A geometrically thin shell will have a high peak-to-center ratio; this is not seen in these observations, suggesting that the shell is radially extended. If IRAS 07134+1005 has undergone a sudden ejection, the ejecta would be seen as a very thin, high surface brightness shell, since it is expected to be optically thin in the mid-infrared wavelengths. The observed profile is instead consistent with an extended stellar wind but not a thin, dense shell. The model is slightly brighter than the observations in the outer regions, suggesting that the mass loss was actually slightly less in the past than that of the model, which assumes $\rho \propto r^{-2.5}$.

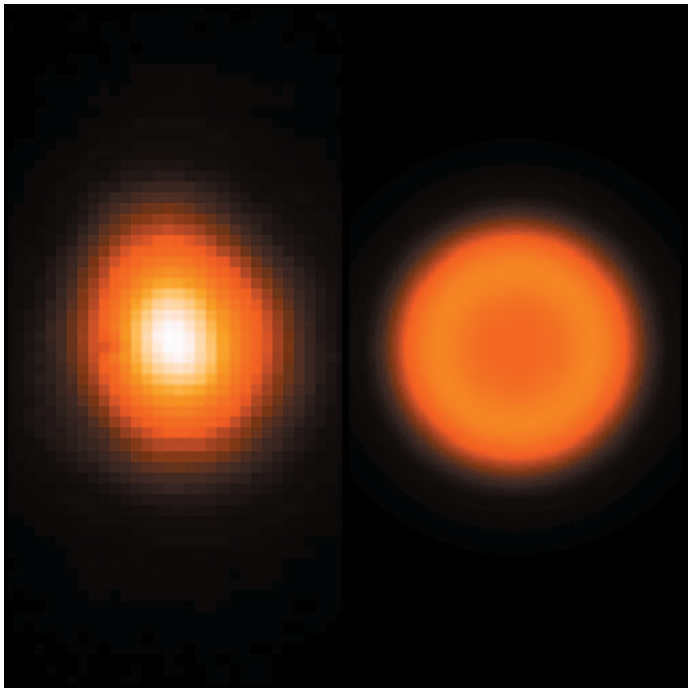

FIG. 7*a*

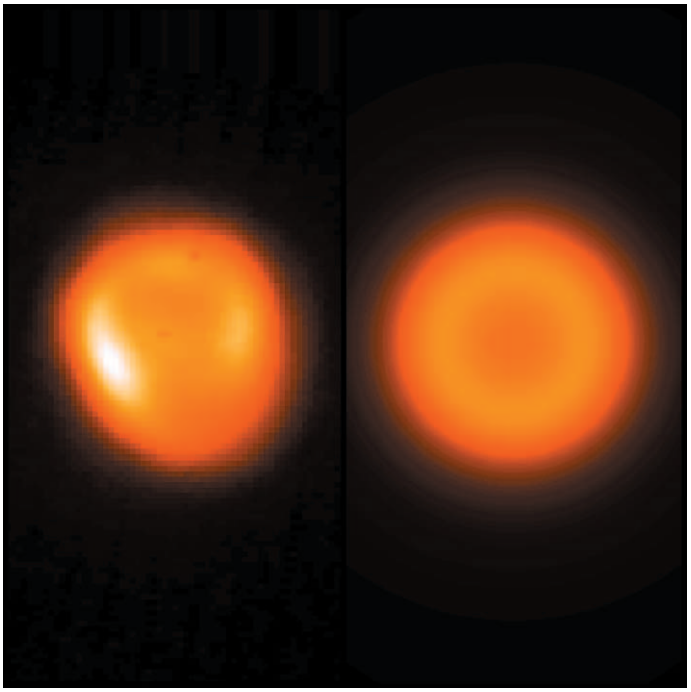

FIG. 7*b*

FIG. 7.—Comparison between the observed 10.3 μm image (*a*) and a 10.6 μm model image derived from a one-dimensional radiation transfer model fitted to the observed SED (*b*). The model image is obtained by convolving the intensity profile with a Gaussian of 0.″39 FWHM. Both images are plotted using the same absolute intensity scale. The central star (a point source in the model) is not plotted in the model image. (*a*): IRAS Z02229+6208; (*b*): IRAS 07134+1005.

The derived mass-loss rates for both objects are similar to the mass-loss rates observed in low-mass AGB stars, with no indication that these two objects have undergone any large-scale sudden ejection. The success in fitting the observed images confirms that the dust shells in both objects originate from the remnants of the AGB wind, which ceased about 1000 yr ago in these two objects. The fact that the dust shell of IRAS Z02229+6208 is more compact than that of IRAS 07134+1005 could be due to several reasons. The former object may be located at a larger distance, and in fact Reddy, Bakker, & Hrivnak (1999) determine a distance greater than 2.2 kpc (based on interstellar absorption lines in the spectrum). It may also be the case that IRAS Z02229+6208 is less evolved; it has a spectral type of G8–K0 0–Ia (Hrivnak & Kwok 1999), compared with a spectral type of F5 I for IRAS 07134+1005.

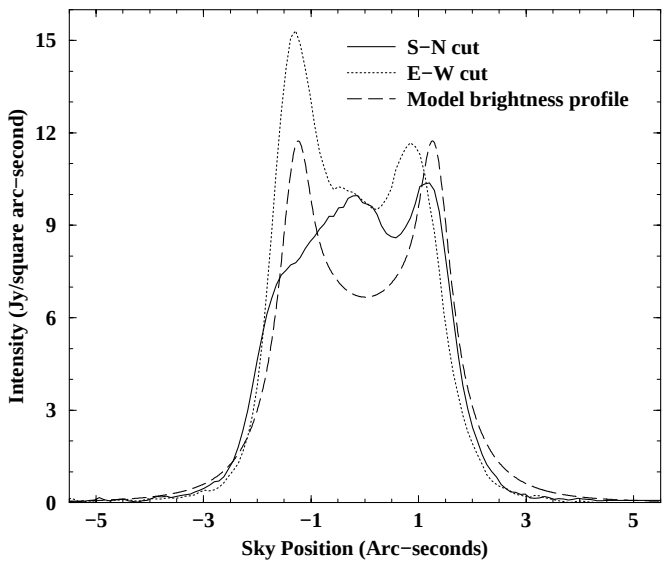

FIG. 8.—Comparison between the observed 20.8 μm intensity profiles of IRAS 07134+1005 along east-west and south-north directions through the center and the 20.5 μm intensity distribution as predicted by a model fitted to the observed SED.

5. CONCLUSIONS

We have obtained very high resolution mid-infrared images of two PPNs showing the 21 μm emission feature. The dust shell of IRAS 07134+1005 shows a clear shell structure with two blobs possibly representing the edges of a torus. There are no observable differences in the morphology of the emission regions of the 11.3 and 21 μm features in comparison with the dust continuum, suggesting that the carriers of these substances share the same spatial location and ejection history as the general dust component. There is no evidence that the 21 μm emission is created by a sudden ejection at the end of the AGB, as suggested by von Helden et al. (2000). In contrast, the observed dust shell of IRAS 07134+1005 is consistent with the model predictions of the post-AGB evolution of a typical low-mass star.

These observations demonstrate that large, ground-based infrared telescopes are capable of resolving the circumstellar dust shells of late-type stars. Such mid-infrared images provide complementary information on the structure of PPNs, which previously have been imaged only in scattered light in the visible and near-infrared. The mid-infrared images also have the potential of clarifying the relationship between the dust torus and the optical, often bipolar, reflection nebulae, therefore providing important clues on the physical origin of the shaping of PNs.

We thank Stephanie Côté for carrying out the Gemini Quickstart observations. This work is supported by grants to S. K. and K. V. from the Natural Science and Engineering Research Council of Canada and a grant to B. J. H. from the National Science Foundation (AST 99-00846). S. K. acknowledges the award of a Killam Fellowship from the Canada Council for the Arts.

REFERENCES

Aaquist, O. B., & Kwok, S. 1996, ApJ, 462, 813
Bakker, E. J., van Dishoeck, E. F., Waters, L. B. F. M., & Schoenmaker, T. 1997, A&A, 323, 469
Bryce, M., Balick, B., & Meaburn, J. 1994, MNRAS, 266, 721
Buss, R. H., et al. 1990, ApJ, 365, L23
Dayal, A., Hoffmann, W. F., Bieging, J. H., Hora, J. L., Deutsch, L. K., & Fazio, G. G. 1998, ApJ, 492, 603
Grishko, V. I., Tereschuk, K., Duley, W. W., & Bernath, P. 2001, ApJ, 558, 129
Hill, H. G. M., Jones, A. P., & d'Hendecourt, L. B. 1998, A&A, 336, L41
Hrivnak, B. J. 1995, ApJ, 438, 341
Hrivnak, B. J., & Kwok, S. 1999, ApJ, 513, 869
Hrivnak, B. J., Volk, K., & Kwok, S. 2000, ApJ, 535, 275
Jura, M., Chen, C., & Werner, M. W. 2000, ApJ, 544, L141
Kwok, S. 1993, ARA&A, 31, 63
Kwok, S., Hrivnak, B. J., & Geballe, T. R. 1995, ApJ, 454, 394
Kwok, S., Volk, K., & Bernath, P. 2001, ApJ, 554, L87
Kwok, S., Volk, K. M., & Hrivnak, B. J. 1989, ApJ, 345, L51
———. 1999a, A&A, 350, L35
———. 1999b, in IAU Symp. 191, Asymptotic Giant Branch Stars, ed. T. Le Bertre, A. Lébre, & C. Waelkens (San Francisco: ASP), 297
Meixner, M., Skinner, C. J., Graham, J. R., Keto, E., Jernigan, J. G., & Arens, J. F. 1997, ApJ, 482, 897
Papoular, R. 2000, A&A, 362, L9
Reddy, B. E., Bakker, E. J., & Hrivnak, B. J. 1999, ApJ, 524, 831
van Winckel, H., & Reyniers, M. 2000, A&A, 354, 135
Volk, K., Kwok, S., & Hrivnak, B. J. 1999, ApJ, 516, L99
von Helden, G., et al. 2000, Science, 288, 313
Webster, A. 1995, MNRAS, 277, 1555